



Niobium carbide MXenzyme-Driven comprehensive cholesterol regulation for photoacoustic image-guided and anti-inflammatory photothermal ablation in atherosclerosis

Wenqi Pan^{a,1}, Jingyun Cheng^{a,1}, Xinyue Cao^b, Yi Zheng^{a,*}, Zhenyu Yang^b, Wei Feng^{b,****}, Yu Chen^{b,c,***}, Rong Wu^{a,**}

^a Department of Ultrasound, Shanghai General Hospital, Shanghai Jiao Tong University School of Medicine, Shanghai, 200080, PR China

^b Materdicine Lab, School of Life Sciences, Shanghai University, Shanghai, 200444, PR China

^c Shanghai Institute of Materdicine, Shanghai, 200051, PR China

ARTICLE INFO

Keywords:

Atherosclerosis
MXenzyme
Lipid regulation
Anti-inflammation
Theranostics

ABSTRACT

Foam cells play a pivotal role in the progression of atherosclerosis progression by triggering inflammation within arterial walls. They release inflammatory molecules that attract additional immune cells, leading to further macrophage recruitment and plaque development. In this study, we develop an osteopontin (OPN) antibody-conjugated niobium carbide (Nb₂C-aOPN) MXenzyme designed to selectively target and mildly ablate foam cells while reducing inflammation in the plaque microenvironment. This approach utilizes photonic hyperthermia to decrease plaque size by enhancing cholesterol regulation through both passive cholesterol outflow and positive cholesterol efflux. Nb₂C-aOPN MXenzyme exhibits multiple enzyme-mimicking properties, including catalase, superoxide dismutase, peroxidase and glutathione peroxidase, and acts as a scavenger for reactive oxygen and nitrogen species. The inhibition of reactive oxygen and nitrogen species synergizes with photothermal ablation to promote positive cholesterol efflux, leading to reduced macrophage recruitment and a shift in macrophage phenotype from M1 to M2. This integrative strategy on cholesterol regulation and anti-inflammation highlights the potential of multifunctional 2D MXenzyme-based nanomedicine in advancing atherosclerotic regression.

1. Introduction

Atherosclerosis, a chronic and progressive cardiovascular disease, is a significant global health issue due to its high prevalence and impact on morbidity and mortality [1]. This disease begins with inflammation driven by atherogenic lipoproteins, which impair endothelial function. In response, cholesterol and lipids accumulate in the arterial walls and are engulfed by macrophages, forming foam cells—a key feature of atherosclerotic plaques [2]. Over time, the persistent accumulation of foam cells and inflammatory mediators leads to plaque growth, arterial narrowing, reduced blood flow, and the risk of severe complications

such as myocardial infarction and stroke [2,3]. Current pharmacological interventions such as lipid-lowering or anti-inflammatory drugs stabilize plaques [4,5], but their effectiveness in plaque regression is not fully established. Additionally, long-term pharmacotherapy may pose risks of adverse effects, drug interactions, and patient non-compliance [6]. Surgical treatments, while effective in plaque removal, are invasive [7, 8]. Consequently, there is a pressing need for a non-invasive treatment approach that can remove plaques and relieve vascular stenosis.

Photothermal therapy (PTT) is an emerging therapeutic approach that utilizes photothermal conversion agents to locally generate heat, selectively destroying diseased tissues [9,10]. Researches have

Peer review under responsibility of KeAi Communications Co., Ltd.

* Corresponding authors.

** Corresponding author.

*** Corresponding author. Materdicine Lab, School of Life Sciences, Shanghai University, Shanghai, 200444, PR China.

**** Corresponding author.

E-mail addresses: zhengyichn@sjtu.edu.cn (Y. Zheng), fengw@shu.edu.cn (W. Feng), chenyuedu@shu.edu.cn (Y. Chen), wurong7111@sjtu.edu.cn (R. Wu).

¹ These authors contributed equally to this work.

<https://doi.org/10.1016/j.bioactmat.2024.07.001>

Received 28 March 2024; Received in revised form 30 June 2024; Accepted 2 July 2024

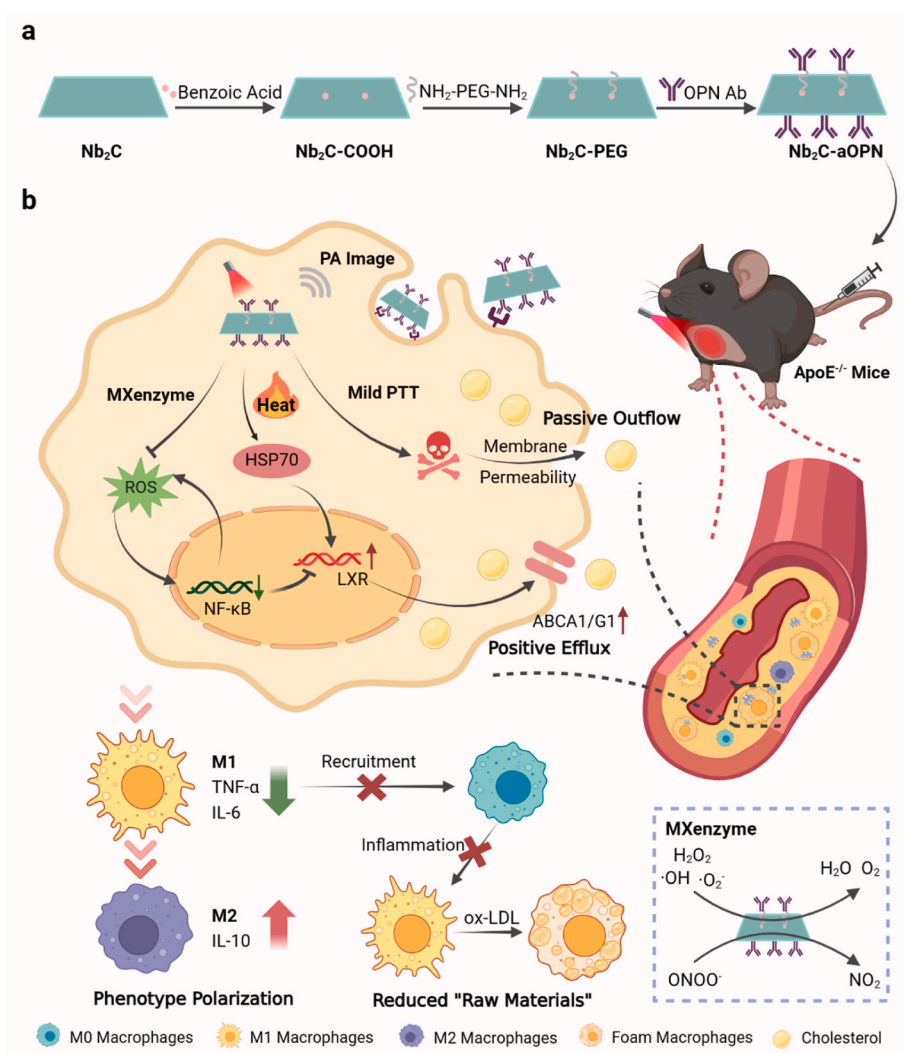
2452-199X/© 2024 The Authors. Publishing services by Elsevier B.V. on behalf of KeAi Communications Co. Ltd. This is an open access article under the CC BY-NC-ND license (<http://creativecommons.org/licenses/by-nc-nd/4.0/>).

demonstrated the successful regression of atherosclerosis through the photothermal ablation of inflammatory macrophages [11–13] and foam cells [14]. However, this process can exacerbate existing inflammation by producing reactive nitrogen and oxygen species (RNOS), potentially leading to the reformation of plaques under hyperlipidemic conditions—a phenomenon akin to the “recurrence” of the “residual fire” in treated area. Efforts have been made to alleviate inflammation [15]. Nanozymes, nanomaterials with enzyme-mimicking activity [16–18], have emerged as a versatile solution in various biomedical fields, including atherosclerotic treatment [19,20]. Their ability to neutralize RNOS minimizes oxidative damage within arterial walls [21,22]. Furthermore, nanozymes can regulate the production of inflammatory mediators, such as cytokines and chemokines, thereby reducing inflammation in atherosclerotic plaques [23,24].

Achieving accurate PTT is crucial. Researchers have developed various methods to target atherosclerotic lesions, using the conjugation of different types of ligands [25,26] and biomimetic techniques [27,28]. Osteopontin (OPN), a secreted phosphorylated glycoprotein, plays a pivotal role in atherosclerotic plaque formation and progression [29]. Unlike the scant expression in normal arterial walls, OPN is markedly overexpressed by foam cells within the subendothelial space [30]. This distinctive expression pattern makes OPN a prime candidate for targeted approaches in atherosclerosis therapy and diagnostics [26,31]. Extensive research has identified OPN as an optimal biomarker for detecting

vulnerable plaques, primarily through imaging techniques that focus on foam cell activities [32].

Based on the aforementioned considerations, in this study, we rationally design and construct an OPN antibody-conjugated niobium carbide (denoted Nb₂C-aOPN). Nb₂C possesses the ability to absorb laser pulses, converting them to heat and subsequently generating acoustic waves, which can be detectable by ultrasonic transducers and can be reconstructed into photoacoustic (PA) images [33]. Owing to its high photothermal conversion efficacy, Nb₂C is regarded as an efficient photothermal agent and a potent PA contrast agent [34]. Nb₂C-aOPN facilitates passive cholesterol outflow through PA image-guided photothermal ablation, by enhancing membrane permeability. Additionally, as a MXene-based nanozyme (MXenzyme), the nanoconstruct exhibits multiple enzyme-mimicking properties and effectively scavenge RNOS [35]. At the lesion site, it modulates macrophage recruitment and phenotype polarization. Notably, *in vitro* experiments demonstrate a synergistic effect of Nb₂C-aOPN in combining anti-inflammatory and photothermal treatments to promote positive cholesterol efflux. (Scheme 1). The anti-atherosclerotic efficacy of Nb₂C-aOPN is further validated in an atherosclerotic ApoE^{-/-} mouse model, highlighting its unique properties and functions in atherosclerosis management. This study deliberately incorporates both photothermal therapy and anti-inflammatory approaches to explore a comprehensive treatment strategy for atherosclerosis.



Scheme 1. Scheme of the fabrication of the Nb₂C-aOPN and its therapeutic mechanism in atherosclerosis. (a) The preparation process of Nb₂C-aOPN. (b) Nb₂C-aOPN as a theranostic agent for PA image-guided atherosclerosis treatment.

2. Results and discussion

2.1. Synthesis, characterization and photothermal performance of Nb₂C-aOPN

2D Nb₂C MXene was synthesized using a chemical exfoliation technique, involving selective etching to aluminum (Al) layer and tetrapropylammonium hydroxide (TPAOH) intercalation (Fig. 1a) [36]. Scanning electron microscopy (SEM) images reveal that the multi-layered Nb₂C exhibits a loose accordion-like morphology, in contrast to the compacted layered microstructure in Nb₂AlC ceramics (MAX phase) (Fig. 1b). Energy-dispersive X-ray (EDX) analysis confirms a reduced amount of Al in multi-layer Nb₂C (Fig. S1). Transmission electron microscopy (TEM) images demonstrate the successfully exfoliated Nb₂C with the ultrathin and electron-transparent structure (Fig. 1c). Atom force microscopy (AFM) measurement further indicates the fabrication of freestanding Nb₂C with a thickness of 4.2 nm, which is indexed to few-layer Nb₂C (Fig. 1d).

To ensure the covalent bonding of the OPN antibody, carboxyl functional groups were initially grafted onto the Nb₂C by utilizing diazonium salt to form Nb₂C-COOH [37]. Subsequently, bifunctional amine polyethylene glycol (NH₂-PEG-NH₂) was linked to Nb₂C-COOH through an amidation reaction. After that, Nb₂C-aOPN was synthesized by linking OPN to Nb₂C-PEG-NH₂ (denoted Nb₂C-PEG) with a hetero-bifunctional crosslinker, succinimidyl-4-(N-maleimidomethyl) cyclohexane-1-carboxylate (SMCC) [38]. Fourier-transform infrared (FTIR) show that the peaks at 1710 cm⁻¹ is assigned to C=O stretching vibration of Nb₂C-COOH. Successful attachment of PEG to Nb₂C-COOH is indicated by the presence of a characteristic peak at 1100 cm⁻¹ of C-O-C from PEG (Fig. 1e). The emergence of the vibrational peak related to the aromatic group of SMCC (Fig. S2) and the observation of multiple bands corresponding to the heavy and light chains of OPN antibody of Nb₂C-aOPN on sodium dodecyl sulfate polyacrylamide gel electrophoresis result (Fig. S3) indicate the successful conjugation of OPN. The changes in zeta potential also indicate the successful modification (Fig. 1f). The content of NH₂-PEG-NH₂ is calculated to be 84.1 μg per 1 mg Nb₂C-aOPN, while the content of aOPN is calculated to be 9.0 μg per 1 mg Nb₂C-aOPN through thermogravimetric analysis. The coupling efficiency of aOPN is 86.2 % (Fig. S4). TEM images show the few-layered Nb₂C-aOPN, with an average size of around 180 nm (Fig. S5a). EDX analysis reveals the emergence of sulfur (S) and nitrogen (N), indicating the successful modification of Nb₂C-aOPN (Fig. S5b). Additionally, Nb₂C-aOPN exhibits high dispersibility in water, phosphate buffer saline (PBS), and culture medium (Fig. S6), providing a possibility for further *in vivo* applications.

Furthermore, the photothermal performance of Nb₂C-aOPN was validated. The absorption spectra of Nb₂C-aOPN show a broad absorption band in the near-infrared (NIR) region, and the extinction coefficient at 808 nm is 7.74 L g⁻¹ cm⁻¹, implying the potential of Nb₂C-aOPN as a photothermal agent (Fig. S7). When different concentrations of Nb₂C-aOPN were exposed to 808 nm laser for 10 min, a significant concentration-dependent temperature rise is observed. In contrast, the change of pure water is not obvious, indicating that Nb₂C-aOPN can quickly and efficiently convert 808 nm NIR light energy into heat energy (Fig. S8a). The photothermal capability of Nb₂C-aOPN further displays the laser-power-dependent photothermal effect (Fig. S8b). These findings demonstrate the potential of excellent control over heat generation. The photothermal conversion efficiency was calculated to be 28.51 % based on the heating and cooling curves (Fig. 1g and S9) [39]. Notably, Nb₂C-aOPN exhibits remarkable thermal and optical stability, as it did not degrade after four cycles of heating and cooling under continuous laser irradiation with a total irradiation time of 20 min (Fig. 1h and S10). Additionally, the irradiation of Nb₂C-aOPN with 808 nm laser results in PA signal generation. The PA intensity increases with elevating concentration of Nb₂C-aOPN and is stable over irradiation time (Fig. S11), indicating its potential as a PA contrast agent for guiding the

irradiation location and enhancing the accuracy of photothermal therapy (Fig. 1i).

2.2. RNOS-scavenging ability of Nb₂C-aOPN

To validate the RNOS-scavenging property of Nb₂C-aOPN, we assessed its total antioxidant ability by measuring the scavenging of 2,20-azinobis (3-ethylbenzthiazoline-6-sulfonate) (ABTS^{•+}), 1,1-diphenyl-2-picrylhydrazyl (DPPH[•]), and 2-phenyl-4,4,5,5-tetramethylimidazole-1-oxyl 3-oxide (PTIO[•]) radicals. The ABTS^{•+} radical was obtained by the oxidation of ABTS with potassium persulfate (Fig. 2a). The antioxidant capacity was assessed by measuring the decrease in absorbance at 734 nm. As depicted in Fig. 2b and S12, the concentration-dependent ability of Nb₂C-aOPN to scavenge ABTS^{•+} radical is evident, with an inhibition rate of up to 95 % at 200 ppm. For the DPPH[•] radical-scavenging experiment, DPPH solid was dissolved in ethanol, and the change in absorbance at 519 nm was measured (Fig. 2c). At a Nb₂C-aOPN concentration of 400 ppm, the inhibition rate of DPPH[•] reaches 75 % (Fig. 2d and S13). Beyond these nitrogen-centered radicals, the PTIO[•] radical is a stable, hydrophilic, oxygen-centered free radical (Fig. 2e). It is observed that the clearance ability of PTIO[•] increases with elevating Nb₂C-aOPN concentration (Fig. S14). Notably, under acidic conditions, the inhibitory effect of Nb₂C-aOPN is intensified (Fig. 2f).

As a typical nanozyme, Nb₂C-aOPN MXenzyme can imitate diverse natural enzymes [40–43]. Superoxide dismutase (SOD) is an enzyme that catalyzes the dismutation of superoxide anion (•O₂⁻) into oxygen (O₂) and hydrogen peroxide (H₂O₂), converting damaging free radicals to less harmful products. The SOD-mimic activity was verified using nitroblue tetrazolium (NBT), which forms an insoluble blue formazan compound when reduced by •O₂⁻. The amount of formazan markedly decreased with increasing Nb₂C-aOPN concentration, confirming the SOD-mimic property of Nb₂C-aOPN (Fig. 2g). This result is further corroborated by the electron spin resonance (ESR) spectra, where the characteristic peak intensity of •O₂⁻ at a rate of 1:1:1:1 dramatically decline with the presence of Nb₂C-aOPN (Fig. 2h). Catalase (CAT) decomposes H₂O₂ into water (H₂O) and O₂, contributing to H₂O₂ detoxification within living cells [40]. The CAT-mimic activity of Nb₂C-aOPN was evaluated through H₂O₂ consumption and O₂ generation. As demonstrated in Fig. 2g, the reduction in H₂O₂ levels correlates with the Nb₂C-aOPN concentration (Fig. 2i). Subsequently, the dissolved oxygen meter detects a 21 mg/L increase in dissolved oxygen level in the solution containing 500 ppm of Nb₂C-aOPN (Fig. 2j).

Peroxidase (POD) is an enzyme that catalyzes the oxidation of substrates such as 3,5,3',5'-tetramethylbenzidine (TMB) by using H₂O₂ as an electron acceptor. In the presence of Nb₂C-aOPN, colorless TMB converts into blue-colored oxidized TMB, leading to increased absorbance at 652 nm over time (Fig. 2k). Moreover, the POD-mimic activity of Nb₂C-aOPN exhibits dose-dependence (Fig. 2l). Additionally, GPx can reduce hydroperoxides to non-toxic alcohols via glutathione (GSH). Glutathione peroxidase (GPx) catalyzes the production of oxidized glutathione (GSSG) from GSH, and GSH reductase (GR) uses nicotinamide adenine dinucleotide phosphate (NADPH) to catalyze GSH production from GSSG. GPx activity was determined by measuring the decrease in NADPH levels at an absorbance of 340 nm (Fig. 2m).

Furthermore, Nb₂C-aOPN can scavenge free radicals, such as hydroxyl (•OH) and peroxynitrite (ONOO⁻). •OH, generated via the Fenton reaction, oxidizes the Fe²⁺ ions in the 1,10-phenanthroline-Fe²⁺ solution to Fe³⁺, leading to a decrease in absorbance at 536 nm. The inhibition of the decrease of the absorbance at 536 nm (Fig. 2n) and corresponding quantification result (Fig. S15) reflect the capacity of Nb₂C-aOPN to scavenge •OH. ESR result (Fig. 2o) further confirms the •OH scavenging ability. Besides, approximately 37.5 % of ONOO⁻ is eliminated by Nb₂C-aOPN at the concentration of 100 ppm (Fig. 2p).

Considering the typically weakly acidic nature of inflammatory environments [44], we tested the RNOS-scavenging ability of Nb₂C-aOPN

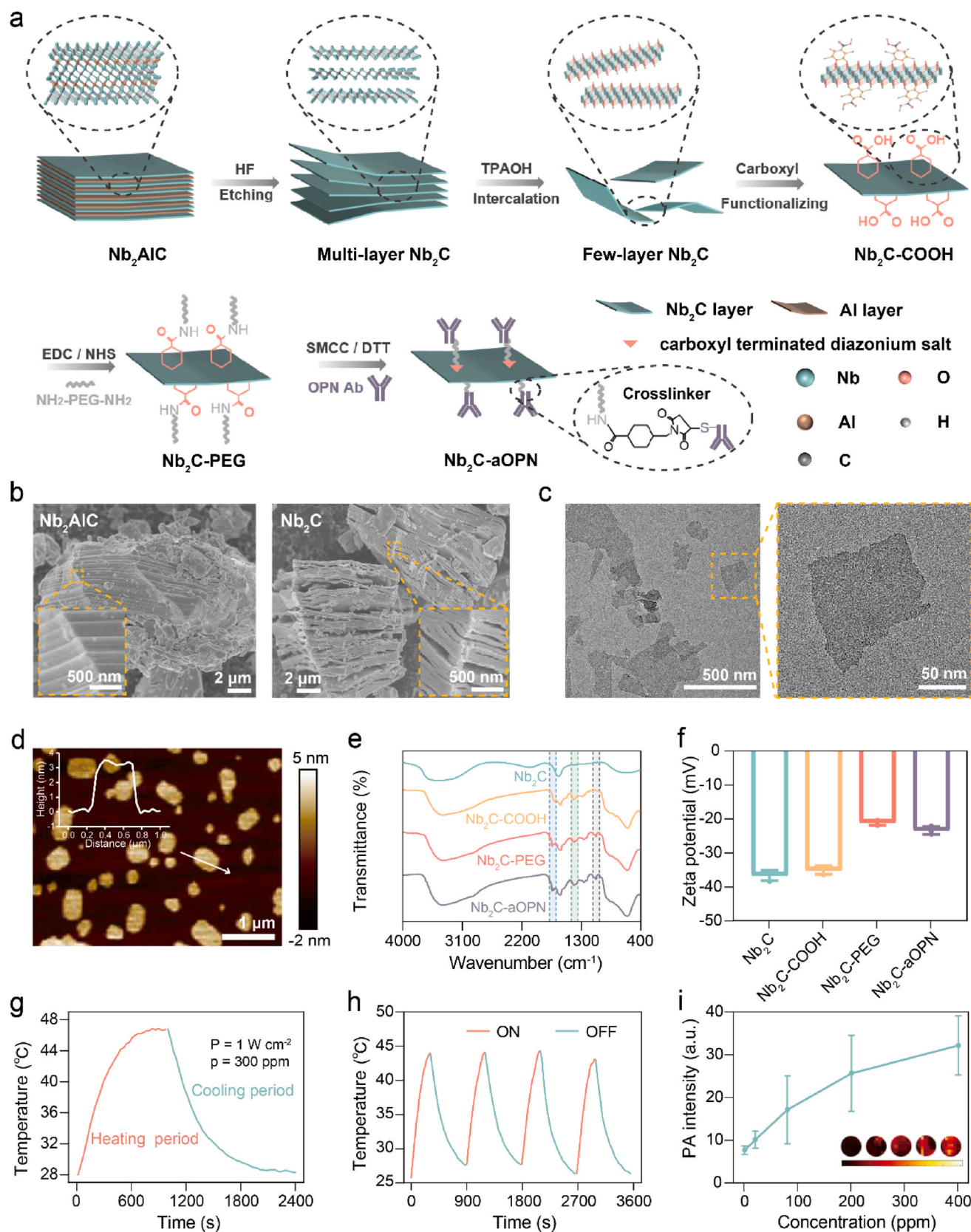


Fig. 1. Synthesis, characterization and Photothermal Performance of Nb₂C-aOPN. (a) Schematic preparation of Nb₂C-aOPN. (b) SEM images of the bulk Nb₂AlC and the multi-layer Nb₂C. Inset images depict the corresponding high-magnification SEM image. (c) TEM images of few-layer Nb₂C. (d) AFM image of few-layer Nb₂C. (e) FTIR spectra of Nb₂C, Nb₂C-COOH, Nb₂C-PEG and Nb₂C-aOPN. (f) Zeta potential of Nb₂C, Nb₂C-COOH, Nb₂C-PEG and Nb₂C-aOPN. (g) Photothermal performance of Nb₂C-aOPN (300 ppm) under 808 nm irradiation (1 W/cm²). (h) Heating curves of Nb₂C-aOPN (300 ppm) for four on/off cycles under 808 nm irradiation (1 W/cm²). (i) Quantitative photoacoustic intensity at 808 nm for Nb₂C-aOPN with different concentrations. Data in (f) and (i) are expressed as means ± SD (n = 3).

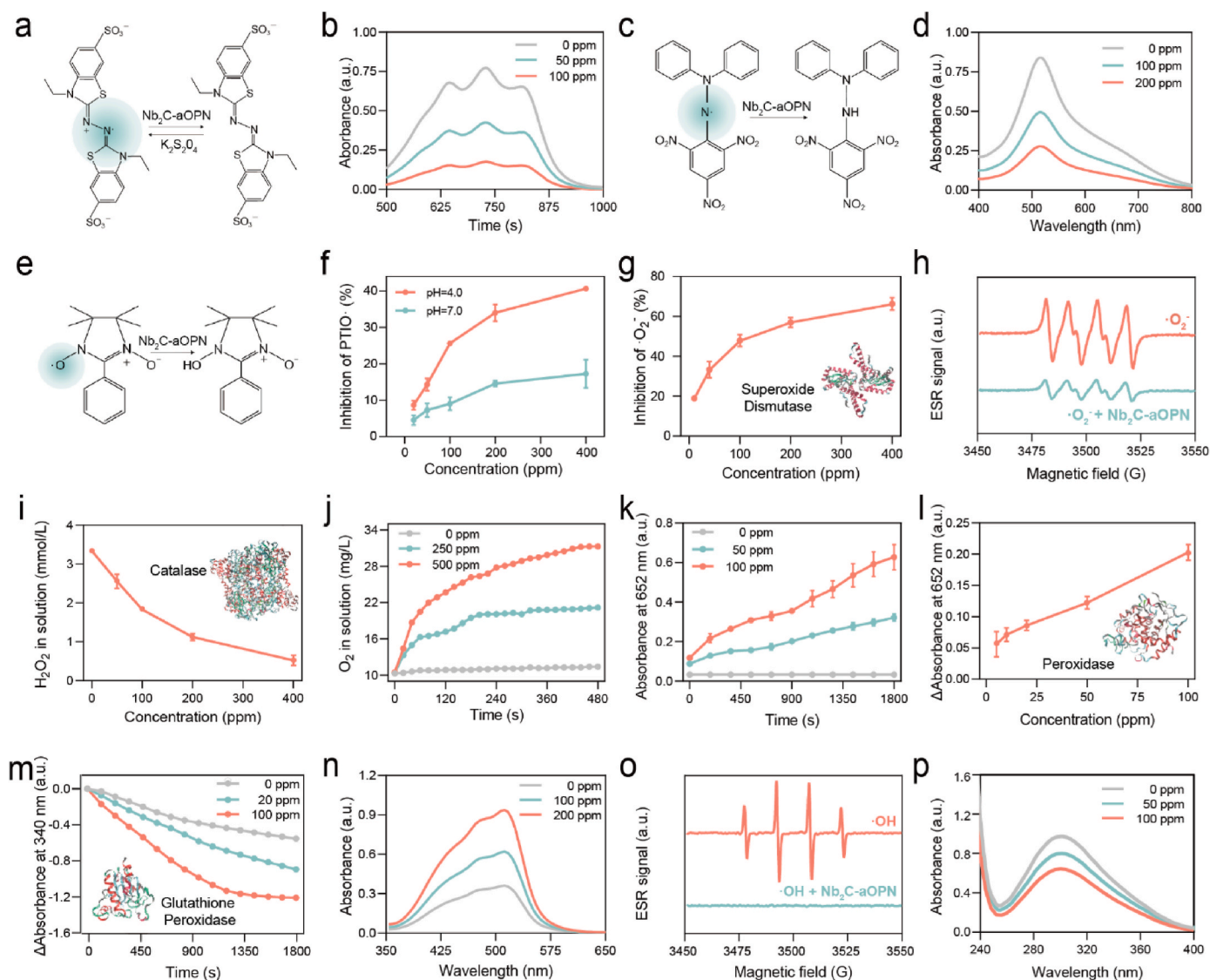


Fig. 2. RNOS-scavenging property of Nb₂C-aOPN. (a) Illustration and (b) UV–vis absorption results of ABTS^{•+} radical-scavenging property of Nb₂C-aOPN. (c) Illustration and (d) UV–vis absorption results of DPPH[•] radical-scavenging property of Nb₂C-aOPN. (e) Illustration and (f) quantitative inhibition rates of PTIO[•] radical. (g) SOD-mimic property of Nb₂C-aOPN. (h) ESR results for •O₂⁻ inhibition. (i) Quantification of H₂O₂ decomposition catalyzed by Nb₂C-aOPN. (j) CAT-mimic property of Nb₂C-aOPN in the production of oxygen from H₂O₂ within 8 min. (k) Reaction-time curves of the TMB colorimetric reaction catalyzed by Nb₂C-aOPN. (l) Concentration-dependent POD-mimic property of Nb₂C-aOPN. (m) GPx-mimic property of Nb₂C-aOPN at different concentrations. (n) UV–vis absorption results and (o) ESR results for •OH elimination. (p) UV–vis absorption results of Nb₂C-aOPN on scavenging ONOO⁻. Data in (h, i, k, l and m) are expressed as means ± SD (n = 3).

under acidic condition. Specifically, it is reported that the pH with plaque lesion areas is around 5.5 [45]. Our investigation reveals that Nb₂C-aOPN exhibits a remarkably enhanced RNOS-scavenging capability at pH 5.5 compared to pH 7 (Fig. S16). This notable increase in scavenging ability under acidic conditions aligns well with the physiological microenvironment of atherosclerotic plaque, indicating a potential amplification of the anti-inflammatory effects of Nb₂C-aOPN within the lesion location. Meanwhile, there is negligible difference in the inhibition rate of ABTS^{•+}, DPPH[•], and PTIO[•] with and without continuous laser irradiation for 20 min (Fig. S17), indicating that the photonic hyperthermia does not impact the scavenging ability.

2.3. In vitro photothermal effect of Nb₂C-aOPN on macrophage-derived foam cells

Macrophage-derived foam cells constitute the main component of lipid core in atherosclerotic plaques. Precise elimination of foam cells

can effectively reduce the plaque size without compromising the structural integrity of the fibrous cap, which is essential for plaque stability. Therefore, the cellular uptake levels were determined. Foam cells were successfully induced by lipopolysaccharide (LPS) and oxidized low-density lipoprotein (ox-LDL), while inflammatory macrophages were successfully induced by LPS (Fig. S18). The lipid in foam cells was labeled with Nile Red. Confocal laser scanning microscopy (CLSM) shows significant signal in foam cells after a 2 h incubation of FITC-labeled Nb₂C-aOPN, indicating the internalization of the MXenzyme. The co-localization of Nb₂C-aOPN and lipid content may be attributed to the simultaneous endocytosis. Meanwhile, weak fluorescence signal is observed in inflammatory macrophages resulting from the enhanced phagocytosis of inflammatory macrophage. In contrast, no fluorescence is detected in endothelial cells and pristine macrophages (Fig. 3a and S19). Foam cells were employed to assess the binding affinity of Nb₂C-aOPN. Preincubation with aOPN remarkably reduced uptake by these cells, which demonstrates the selective targeting ability of the antibody

conjugated on the surface of Nb₂C-aOPN (Figs. S20 and S21). This result underscores the specificity of Nb₂C-aOPN with its target, affirming the role of the surface antibody in mediating selective cellular engagement. The effect of aOPN content on cellular uptake was determined. An aOPN content of 13.1 µg per 1 mg Nb₂C-aOPN shows the highest uptake; however, the coupling efficacy is only 62.7 %, which represents a waste of resources (Fig. S22). The Nb₂C-aOPN demonstrates negligible

cytotoxicity towards foam cells and inflammatory macrophages even at a concentration of as high as 400 ppm over a 12-h period (Fig. 3b). Subsequently, foam cells were incubated with Nb₂C-aOPN at a concentration of 200 ppm for 4 h, followed by an 808 nm laser radiation at 1 W/cm² for 10 min. Live and dead cells were distinguished using Calcein-AM and PI co-staining. Remarkably, the Nb₂C-aOPN + NIR group exhibits a significant decrease in cell viability, while neither

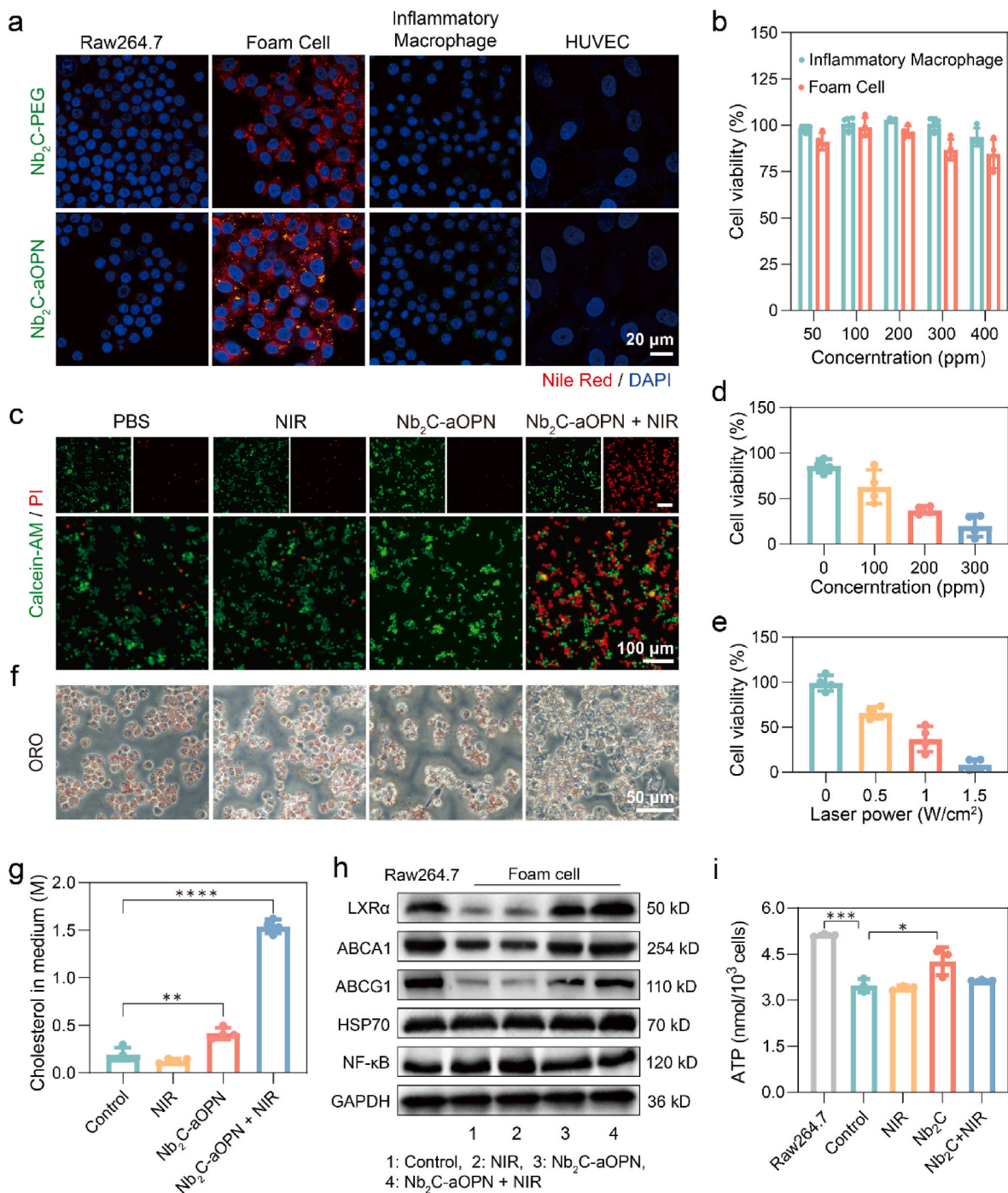


Fig. 3. *In vitro* photothermal effect and lipid regulation ability of Nb₂C-aOPN. (a) CLSM images of different cell lines after incubation with FITC-labeled Nb₂C-PEG and FITC-labeled Nb₂C-aOPN. (b) Cell viability of foam cells and inflammatory cells incubated with Nb₂C-aOPN at various concentrations. (c) Fluorescent microscopic images of foam cells with different treatments stained with Calcein-AM/PI. Cell viabilities of foam cells after incubation with Nb₂C-aOPN at (d) different concentrations and (e) different laser densities. (f) Optical microscopic images of foam cells under different stimulations with ORO staining. (g) Free cholesterol contents of supernatant of foam cells with different treatments. (h) Western blot bands of LXRα, ABCA1, ABCG1, HSP70 and NF-κB. (i) Intracellular ATP levels of foam cells. Data in (b, d and e) are expressed as means ± SD (n = 4). Data in (g and i) are expressed as means ± SD (n = 3). P values were calculated using one-way analysis of variance (ANOVA). *p < 0.05, **p < 0.01, ***p < 0.001, ****p < 0.0001.

irradiation alone nor Nb₂C-aOPN alone affects cell viability (Fig. 3c). Cell counting kit-8 (CCK-8) assay was further employed to quantify the cell viability, which indicates a reduction of approximately 64 % under the aforementioned conditions. The toxicities observed are dose-dependent and laser power-dependent (Fig. 3d and e), consistent with the photothermal effect of the MXenzyme. Meanwhile, human umbilical vein endothelial cells (HUVECs) are resistant to PTT due to insufficient internalization (Fig. S23). These findings clearly demonstrate the potent PTT ability of Nb₂C-aOPN for foam cell elimination.

Alterations in membrane permeability are closely associated with cell death processes and can contribute to the passive outflow of intracellular cholesterol. Oil red O (ORO) staining results reveal that PTT leads to a decrease in intracellular lipid content (Fig. 3f and S24). Similar result is observed from the Nile Red fluorescence images, and the corresponding mean fluorescence intensity (MFI) analysis provides a semi-quantitative assessment (Fig. S25). It is evident that PTT causes a decrease in intracellular lipid content and a concomitant increase in cholesterol levels in the culture medium (Fig. 3g).

2.4. Lipid regulation by Nb₂C-aOPN

However, an intriguing phenomenon emerges, whereby Nb₂C-aOPN only results in an increase in medium cholesterol levels (Fig. 3g). Given the efficient RNOS-scavenging ability of Nb₂C-aOPN and the fact that inflammation can disrupt cholesterol efflux pathways through various mechanisms [46], we conducted Western Blot analysis to evaluate the expression of key proteins involved in cholesterol efflux and inflammation pathway. As depicted in Fig. 3h, the expression of nuclear factor kappa-light-chain-enhancer of activated B cells (NF-κB) is down-regulated while liver X receptors (LXR) and ATP-binding cassette transporter A1/G1 (ABCA1/G1) are upregulated in both Nb₂C-aOPN and Nb₂C-aOPN + NIR groups, indicating the inhibition of the inflammation pathway and the promotion of the cholesterol efflux pathway.

In particular, the upregulation of LXR and ABCA1/G1 was more pronounced in Nb₂C-aOPN + NIR group (Fig. 3h). Previous studies have explored the application of photothermal approaches in modulating lipid metabolism, consistently involving the participation of heat shock proteins (HSPs) and heat shock factors (HSFs) [14,47]. One specific heat shock protein, HSP70, is a chaperone protein that plays a crucial role in cellular stress responses and is prominently expressed under conditions of 42 °C [48]. HSP70 induces transcriptional re-programming, including the upregulation of LXR and subsequent activation of ABCA1/G1 [49], which aligns with the WB result (Fig. 3h). Since ABCA1/G1 utilize energy from ATP hydrolysis to transport cholesterol across cellular membranes, the presence of ATP is necessary for facilitating cholesterol efflux [50]. Foam cells exhibit reduced intracellular ATP levels compared to pristine macrophages, which is attributed to inflammation and impaired mitochondrial function, a consequence of oxidative stress induced by ox-LDL [51]. Intriguingly, a slight elevation in the intracellular ATP levels is observed in the Nb₂C-aOPN group (Fig. 3i), owing to the protective effects of Nb₂C-aOPN against inflammatory damage. However, the Nb₂C-aOPN + NIR group shows a decrease in intracellular ATP level compared to the Nb₂C-aOPN group, which may be associated with the ATP hydrolysis induced by HSP70 [52]. No differences are observed in extracellular ATP levels (Fig. S26). These results suggest that Nb₂C-aOPN promotes active cholesterol efflux through the LXR signaling pathway, and PTT further enhances this process by inducing the expression of HSP70.

2.5. In vitro anti-inflammatory property of Nb₂C-aOPN

Encouraged by the downregulation of NF-κB in foam cells, we proceeded to investigate the anti-inflammatory property of Nb₂C-aOPN in inflammatory macrophages induced by hydrogen peroxide (H₂O₂) or LPS in raw264.7 cells. To assess the presence of ROS, 2', 7'-dichlorofluorescein diacetate (DCFH-DA) staining was used. CLSM images reveal

significant green signal in inflammatory macrophages, whereas pristine macrophages (control group) exhibit negligible signal. Notably, Nb₂C-aOPN shows distinct ROS-scavenging properties in inflammatory macrophages (Fig. 4a). Quantitative analysis using flow cytometry also confirms reduced intracellular ROS levels (Fig. S27). Similarly, intracellular RNS were evaluated by diaminofluorescein-FM diacetate (DAF-FM) staining, and both CLSM and cytometry analysis reveal a decrease of RNS levels with the coinubation of Nb₂C-aOPN (Fig. 4b and S28).

Macrophages exhibit distinct morphologies and functional characteristics depending on their activation state and the microenvironment they encounter. Inflammatory macrophages treated with Nb₂C-aOPN display a reduction in pseudopodia and adopt a rough surface morphology, indicating a polarization shift from the inflammatory M1 phenotype to the anti-inflammatory M2 phenotype. (Fig. S29). The cytometry results further confirm the polarization of macrophage phenotypes from a biomarker perspective (Fig. 4c and S30). The secretion patterns of cytokines differ among macrophages phenotypes. With the transition from M1 to M2 phenotype resulting from the anti-inflammatory effects of Nb₂C-aOPN, the secretion of pro-inflammatory cytokines such as tumor necrosis factor-alpha (TNF-α) and interleukin-6 (IL-6) are significantly inhibited (Fig. 4d and e) while the secretion of the typical anti-inflammatory cytokine, interleukin-10 (IL-10) is increased (Fig. 4f). The observed variation in IL-10 secretion between the groups treated with LPS and H₂O₂ can be explained by their distinct mechanisms of inflammation induction. H₂O₂ primarily induces inflammation through oxidative stress, which alters the redox state of cells, influencing cytokine production and cellular stress response [53]. In contrast, inflammation triggered by LPS is mediated through Toll-like receptor pathways, which activate robust inflammatory signaling cascades, culminating in a widespread inflammatory response [54]. Although both agents are potent inducers of inflammation, the pathways, cellular responses, and the overall impact of each differ significantly, leading to variable patterns of IL-10 secretion. The increase in IL-10 secretion by raw264.7 macrophages is observed when treated with H₂O₂, which could be interpreted as a form of negative feedback regulation, a cellular response to counterbalance the inflammatory stimuli [55]. Notably, treatment with Nb₂C-aOPN further augmented IL-10 secretion, which is likely attributable to the intrinsic propensity of M2 macrophages, known for their anti-inflammatory functions, to produce IL-10.

In atherosclerotic plaques, the interaction between macrophages and endothelial cells plays a crucial role in the development and progression of the disease. The pro-inflammatory cytokine TNF-α induces inflammation in endothelial cells, leading to the recruitment and adhesion of macrophages to these activated endothelial cells [56]. In this study, a transwell system was used to simulate the interaction of macrophages and endothelial cells (Fig. 4g). Specifically, the supernatant of macrophages with different treatments was collected and added to the lower chamber containing endothelial cells. Pristine M0 macrophages were placed in the upper chamber and the migrated macrophages were subsequently stained with crystal violet. It is evident that Nb₂C-aOPN reduces the recruitment of macrophages (Fig. 4h). The concentration of monocyte chemoattractant protein-1 (MCP-1) in the supernatant of HUVECs provides critical insights into the endothelial cell response to inflammatory stimulation. The findings indicate a pronounced increase in MCP-1 secretion following TNF-α stimulation, thereby facilitating the recruitment of monocytes to the site of inflammation. In contrast, Nb₂C-aOPN treatment demonstrates a notable suppressive effect on the secretion of chemotactic factors, resulting in a subsequent reduction in the recruitment of monocytes (Fig. S31). This reduction can potentially limit the availability of “raw materials” for the formation of inflammatory cells and foam cells.

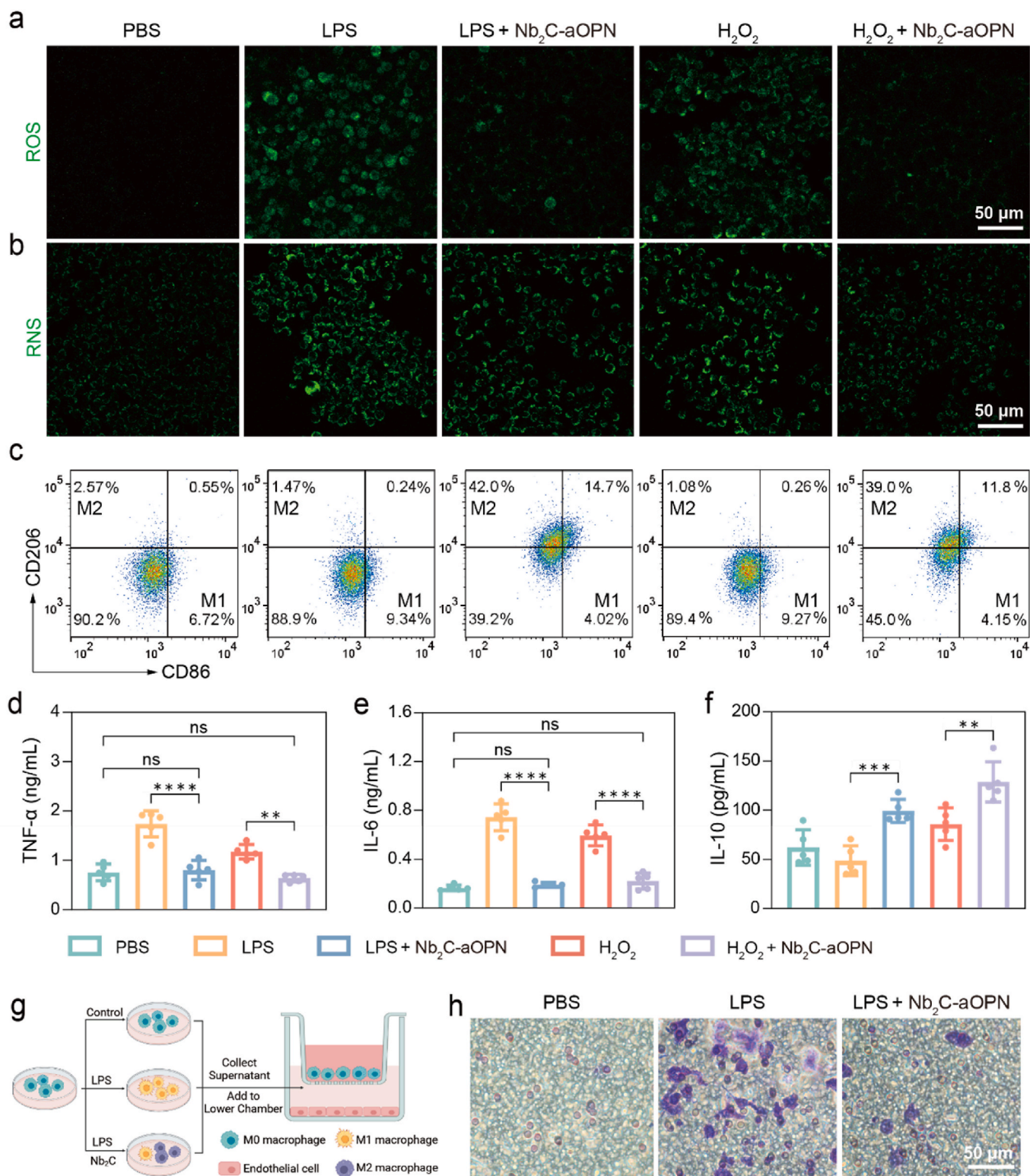


Fig. 4. *In vitro* anti-inflammatory property of Nb₂C-aOPN. Confocal images of (a) ROS and (b) RNS generation in raw264.7 cells under different stimulations. (c) Flow cytometry results of macrophage polarization after different treatments. Secretion levels of (d, e) pro-inflammatory factors (TNF-α and IL-6) and (f) anti-inflammatory factors (IL-10) of raw264.7 cells with different treatments. (g) Experimental setup for the transwell system. (h) Optical microscopy images of migrated raw264.7 cells with crystal violet staining. M0 macrophage refers to raw264.7. Data in (d–f) are expressed as means ± SD (n = 5). P values were calculated using one-way ANOVA. *p < 0.05, **p < 0.01, ***p < 0.0001, ns represents no statistical difference.

2.6. Mechanisms of Nb₂C-aOPN for regulating lipid metabolism and inflammation

To gain further insight into the therapeutic mechanisms in atherosclerosis treatment, high-throughput transcriptomics analysis was performed. The heat map illustrates 566 differentially expression genes (DEGs) between the Nb₂C-aOPN + NIR and the control group (Fig. 5a). The volcano plot shows 566 DEGs, among which 251 are upregulated and 315 are downregulated (Fig. 5b). The *Rela* gene, also known as NF- κ B subunit p65, is downregulated, while *Hspa5*, a member of the HSP70 family, and *Abcg1* gene are upregulated, consistent with the protein-level changes. The enriched chord diagram displays the corresponding Gene Ontology (GO) biological process terms, revealing the inclusion of the processes related to cholesterol metabolic process and regulation of response to external stimulus (Fig. 5c). To identify functional genes, we compared the DEGs with gene sets associated with the cholesterol metabolism and inflammation gene sets. The Venn diagram shows an intersection of 26 functional genes between DEGs and other groups. Within this intersection, 16 genes are associated with inflammation, 8 genes are related to cholesterol metabolism, and 2 genes are associated with the other two gene sets (Fig. 5d).

Subsequently, a bubble diagram of the Kyoto Encyclopedia of Genes and Genomes (KEGG) analysis highlights gene function enrichment, and the TNF signaling pathway, NF-kappa B signaling pathway and lipid and atherosclerosis are highly involved in the treatment process (Fig. 5e). Furthermore, Gene Set Enrichment Analysis (GSEA) revealed significant enrichment of TNF signaling pathway and IL-17 signaling pathway in the control group compared to the Nb₂C-aOPN + NIR treatment group, while fatty acid metabolism was enriched in the Nb₂C-aOPN + NIR treatment group (Fig. 5f). IL-17 is a cytokine that is primarily produced by T-helper 17 (Th17) cells, a subset of CD4⁺ T cells. IL-17 acts on various cell types, including macrophages and endothelial cells, promoting the recruitment of immune cells and influencing immune responses and inflammation. The downregulation of the IL-17 pathway signifies a mitigation of inflammation [57]. These results strongly suggest an association between the treatment and the regulation of genes in these processes. Furthermore, the protein-protein interaction (PPI) analysis reveals that Tnfaip3 is connected with chemokines such as Ccl5, Cxcl2 and Cxcl10, suggesting a potential anti-inflammatory effect of Nb₂C-aOPN + NIR treatment by reducing the recruitment and activation of other immune cells (Fig. 5g).

2.7. In vivo biocompatibility evaluation of Nb₂C-aOPN

The *in vivo* systematic toxicological evaluation of Nb₂C-aOPN was performed on C57BL/6 mice to assess its potential for clinical translation. The mice were sacrificed under euthanasia 14 days after the injection of saline or Nb₂C-aOPN. No significant changes of hematological parameters are observed in the Nb₂C-aOPN group compared to the control group. Blood biochemical indexes display no statistical significance between both control group and Nb₂C-aOPN group, suggesting minimal renal and hepatic toxicity in the tested mice (Fig. S32). Additionally, histological analysis of major organs shows no significant pathological toxicity after intravenous injection Nb₂C-aOPN, confirming negligible histological abnormalities (Fig. S33). The biodegradation of Nb₂C-aOPN holds paramount importance in guaranteeing its high *in vivo* biosafety. UV-vis-NIR absorption spectra analysis of Nb₂C-aOPN dispersion, co-incubated in PBS at different pH levels including 5.5, 7.0, and 8.5, provides valuable insights into the degradation behavior. The results reveal that Nb₂C-aOPN tends to degrade under basic conditions while remaining relative stability in an acidic environment. This degradation pattern is significant as it suggests the potential for sustained therapeutic performance within the atherosclerosis microenvironment with mild acidity (Fig. S34). These findings demonstrate that Nb₂C-aOPN features excellent biocompatibility and support its potential as a safe and promising candidate for clinical applications.

2.8. In vivo photoacoustic imaging enabled by Nb₂C-aOPN

Vulnerable atherosclerotic plaques are specific types of plaques that are prone to rupture and associated with a higher risk of complications, such as myocardial infarction or strokes. The large lipid-rich core, mainly composed of foam cells, is one of the features of vulnerable atherosclerotic plaques [58]. In order to accurately identify foam cells in vulnerable atherosclerotic plaques, a rapid, noninvasive, sensitive, and cost-effective imaging modality is required.

Motivated by the specific targeting property of Nb₂C-aOPN in foam cells, we proceed to investigate its targeting property in atherosclerotic plaques. Equal amounts of Cy5.5-labeled Nb₂C-PEG and Cy5.5-labeled Nb₂C-aOPN were injected to the atherosclerotic mice and the distribution was evaluated through *ex vivo* fluorescence imaging. The fluorescence of aortic arch and thoracic aorta in the Nb₂C-aOPN group is significantly higher than that in the Nb₂C-PEG group, indicating precise targeting ability of Nb₂C-aOPN to atherosclerotic plaques (Fig. 6a and b). No difference in fluorescence is observed between Nb₂C-PEG and Nb₂C-aOPN in the main organs and both Nb₂C-PEG and Nb₂C-aOPN primarily accumulate in the liver (Fig. S35). Decreased fluorescent intensity in aortic roots of atherosclerotic mice, following pretreatment with aOPN highlights the selective targeting property mediated by the antibody (Fig. S36). The circulation of Nb₂C-aOPN in the bloodstream was analyzed following a two-compartment model, in which the blood circulation half-time of Nb₂C-aOPN is calculated to be 2.32 h (Fig. S37). To assess the cellular distribution of Nb₂C-aOPN within the plaque microenvironment, a human plaque sample was subjected to co-incubation with Nb₂C-aOPN. Notably, a significant overlap is observed between PA signal region and lipid-stained region, confirming the specific targeting of Nb₂C-aOPN for foam cells in the plaque microenvironment (Fig. S38).

Based on the atherosclerotic plaque-targeting property and the *in vitro* satisfactory PA imaging ability of Nb₂C-aOPN, we further investigated its potential for *in vivo* PA imaging of atherosclerotic plaques (Fig. 6c). Atherosclerotic mice were subject to PA imaging 4 h after the injection of Nb₂C-PEG and Nb₂C-aOPN. In both sagittal section and transverse sections, clear structures of the carotid arteries are visible on the ultrasound images (gray) in both groups and a robust PA signal (red) is observed in the Nb₂C-aOPN group compared to the Nb₂C-PEG group (Fig. 6d). The PA signal intensity of the Nb₂C-aOPN group is approximately 2.8 times than that of the Nb₂C-PEG group, assessed with the images in transverse sections (Fig. 6e). A three-dimensional (3D) representation of the PA images was reconstructed by utilizing a series of two-dimensional (2D) maximum amplitude projection PA images captured from different depths of the tissue (Fig. 6f and S39). This tomographic approach allows for a comprehensive evaluation of the atherosclerosis and exhibits possibility and efficacy for detecting and monitoring vulnerable plaques.

2.9. In vivo efficacy of Nb₂C-aOPN on plaque progression

Encouraged by the *in vitro* photothermal properties and *in vivo* targeting capabilities of Nb₂C-aOPN, we extended our investigation to *in vivo* photothermal ablation experiments on atherosclerotic mice. Following intravenous (iv) administration of Nb₂C-aOPN in PBS, anesthetized atherosclerotic mice were subjected to an 808 nm irradiation. With the irradiation at the aortic arch, the temperature of the lesion areas escalates from 30 to 43 °C, cooling down to 33 °C after a subsequent 10-min period at room temperature. In contrast, the lesion regions exhibit negligible change under 808 nm irradiation only (Figs. S40 and S41).

To evaluate the *in vivo* therapeutic activity, atherosclerotic mice were divided to 4 groups: NIR, Nb₂C-aOPN, Nb₂C-aOPN + NIR, and saline as a control group. The therapeutic protocol is depicted in Fig. 7a. Following a 16-week period, the mice were subjected to PA imaging. Notably, the PA signal in the Nb₂C-aOPN + NIR group is markedly

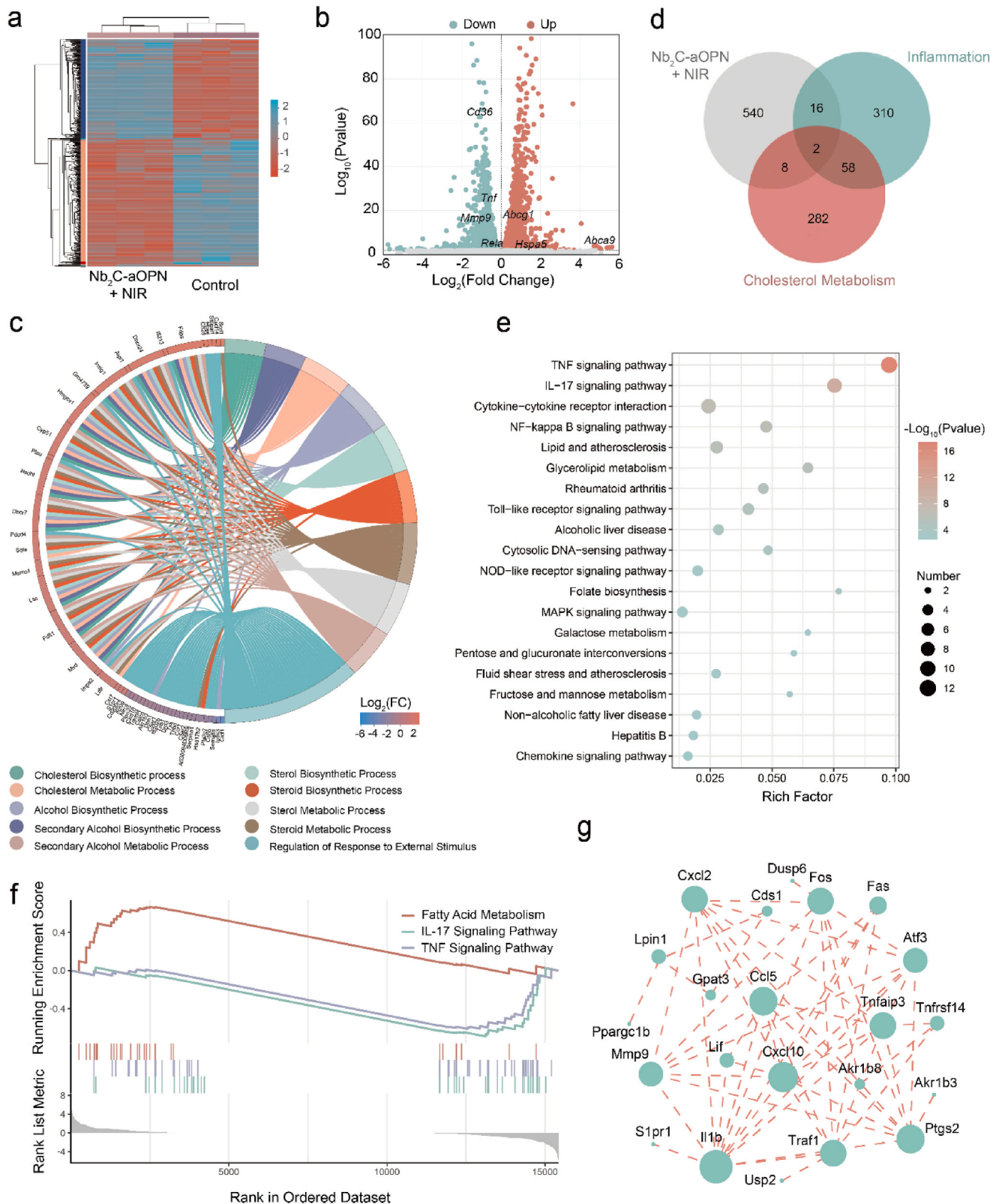


Fig. 5. Therapeutic mechanisms of Nb₂C-aOPN for atherosclerosis treatment by transcriptome high-throughput sequencing. (a) Heat-map diagram of DEGs in foam cells with or without Nb₂C-aOPN + NIR treatment. (b) Volcano plots showing upregulated (red) and downregulated (cyan) genes. (c) Enriched chord diagram of the Gene Ontology (GO) terms based on the DEGs. (d) Venn diagram of transcriptomic profiles among the DEGs, inflammation and lipid metabolism. (e) Kyoto Encyclopedia of Genes and Genomes (KEGG) enrichment analysis of the 26 functional genes in the overlapping region of DEGs and other groups. (f) Topological graph of “fatty acid metabolism”, “IL-17 signaling pathway” and “TNF signaling pathway” mediated by Nb₂C-aOPN + NIR treatment in the Reactome data. (g) Protein-protein interaction network of the 26 functional genes in the intersection.

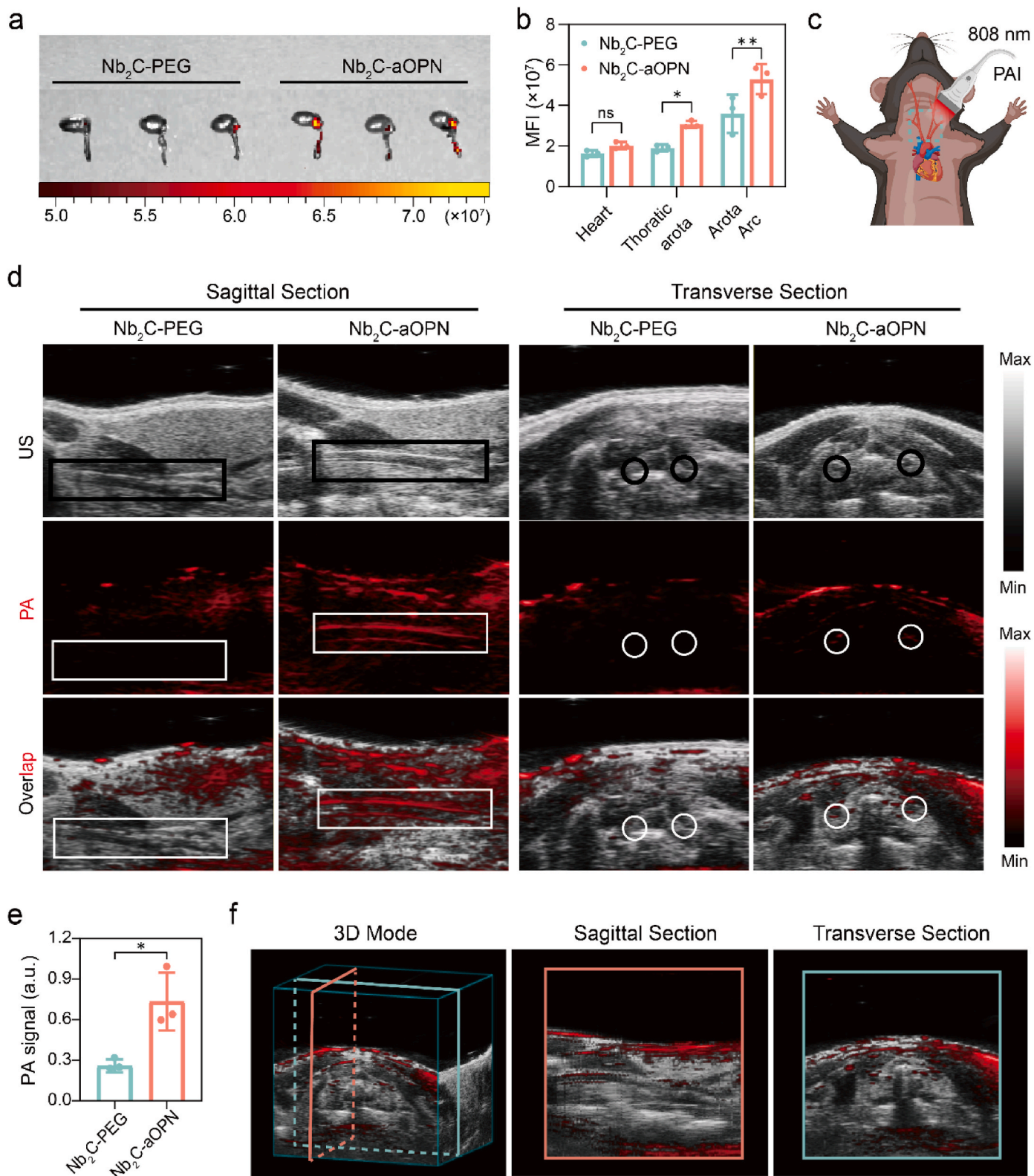


Fig. 6. *In vivo* photoacoustic imaging enabled by Nb₂C-aOPN. (a) *Ex vivo* fluorescence images and (b) quantification of fluorescence intensity in the aortas of atherosclerotic mice. (c) Scheme of Nb₂C-PEG and Nb₂C-aOPN for photoacoustic imaging of atherosclerotic plaques. (d) PA images of sagittal section and transverse section views of atherosclerotic plaques in carotid arteries. (e) Quantitative data of PA intensity of plaques observed in the sagittal section. (f) 3D PA images and corresponding sagittal section and transverse section views of carotid plaques after the injection of Nb₂C-aOPN. Data in (b) and (f) are expressed as means \pm SD ($n = 3$). *P* values were calculated using one-way ANOVA. * $p < 0.05$, ** $p < 0.01$, ns represents no statistical difference.

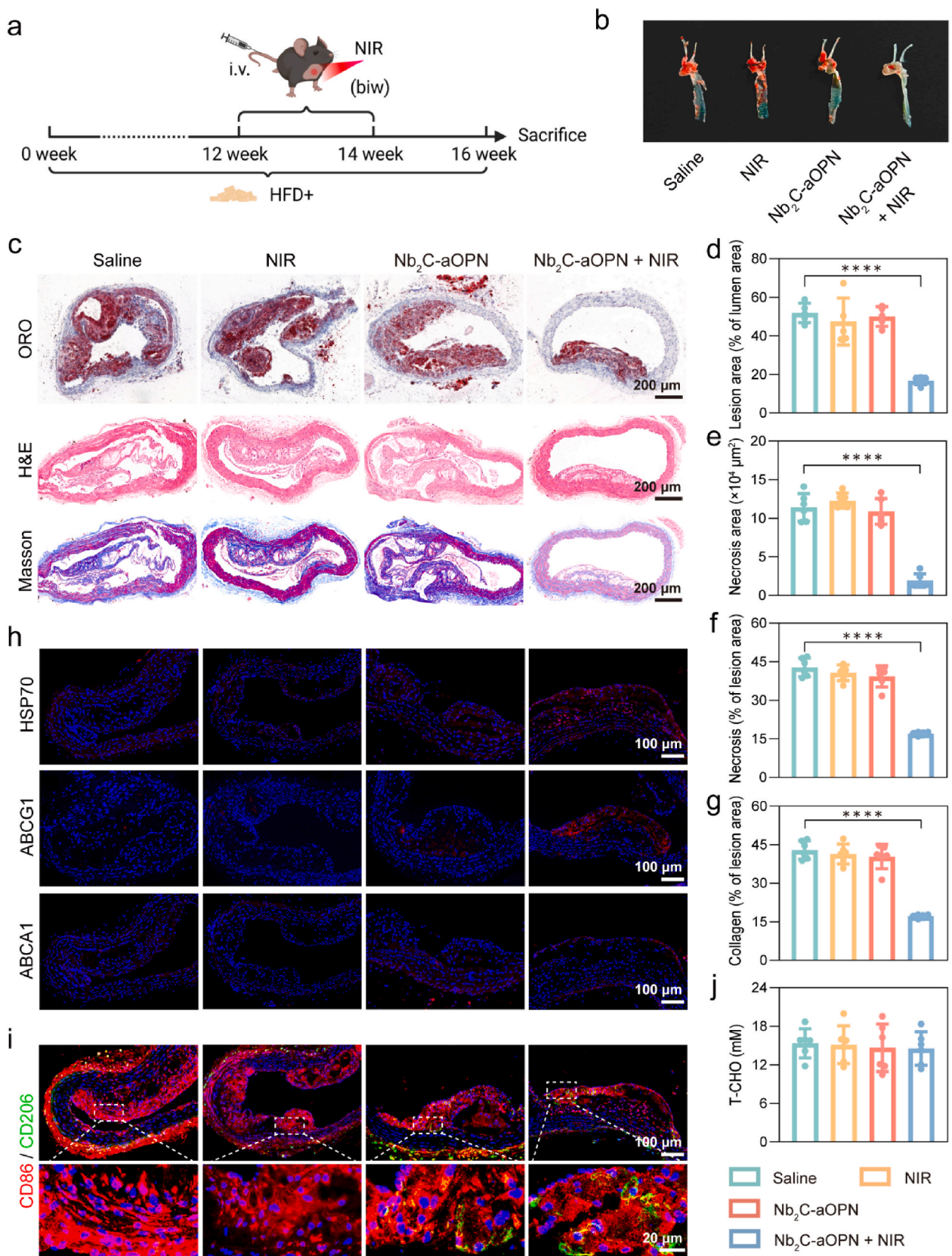


Fig. 7. *In vivo* efficacy of Nb₂C-aOPN on plaque progression. (a) Therapeutic regimen in an atherosclerosis mouse model. (b) Photographs of ORO-stained carotid arteries, aortic arches and thoracic aortas from mice with different treatments. (c) Sections of aortic arches stained by ORO, H&E and Masson's trichrome. Quantitative data of (d) lesion area, (e) lipid area, (f) necrotic core, and (g) collagen in the aortic arch sections. (h) Immunofluorescent staining with HSP70, ABCA1 and ABCG1. (i) Aortic arch sections stained with antibody to CD86 and antibody to CD206. (j) Total cholesterol levels of mice with different treatments. Data in (d, e, f, g and j) are expressed as means ± SD (n = 5). P values were calculated using one-way ANOVA. ****p < 0.0001.

weaker compared to the other groups (Fig. S42). Then, the mice were sacrificed, and their aortas were extracted. The aortas were cut longitudinally to expose the inner wall of the vessels and plaques were stained with ORO. A reduction in plaque area of aortic arch and thoracic aorta is observed in Nb₂C-aOPN + NIR group (Fig. 7b), which corresponds to the results of PA imaging, indicating the potential capability of Nb₂C-aOPN to monitor atherosclerotic plaques. Aortic arch sections were stained with ORO, Hematoxylin & Eosin (H&E), and Masson's trichrome (Fig. 7c) to assess the composition of the plaques. Compared to the control group, Nb₂C-aOPN + NIR significantly reduces the size of plaque, with a noticeable reduction to one-thirds of that in the control group (Fig. 7d). Moreover, both the size and proportion of the necrotic core in the plaques are decreased, with necrotic size measuring 1.9 mm² in Nb₂C-aOPN + NIR compared to 11.4 mm² in the control group, and the necrotic core proportion dropping from 42 % to 17 %. These changes contribute to the enhanced stabilization of the plaques (Fig. 7e and f). Collagen, a byproduct of the inflammatory response, proliferates under inflammatory conditions, leading to fibrosis [59,60]. In the Nb₂C-aOPN + NIR group, there is a diminution of collagen component in the plaques, with a ratio of 2–3 compared to the saline group, which suggests an indication of inflammation remission (Fig. 7g). Despite the observed reduction in collagen content, which is a primary structural component of the fibrous cap, photothermal therapy does not appear to affect the thickness of the fibrous cap, suggesting that the stability of the atherosclerotic plaques remains unchanged post-treatment (Fig. S43).

To investigate the mechanism of the synergic effect of photothermal and anti-inflammatory therapy, immunofluorescence analysis was conducted. It is observed that in the Nb₂C-aOPN + NIR group, HSP70 is activated and the expression of ABCA1/G1 is increased, indicating the potential for enhanced cholesterol efflux (Fig. 7h and Fig. S44). The ROS and RNS levels of the aorta are decreased in both Nb₂C-aOPN and Nb₂C-aOPN + NIR groups (Fig. S45). Additionally, the inflammation mediator, MMP-9, is reduced, attributing to the anti-inflammatory effect of Nb₂C-aOPN (Fig. S46). This inference is further supported by the immunofluorescence staining. Nb₂C-aOPN distinctly converts M1 phenotype of macrophages into M2 phenotype with much reduced CD86 expression and enhanced CD206 expression (Fig. 7i and S47). Moreover, the expression of MCP-1 in both the Nb₂C-aOPN and Nb₂C-aOPN + NIR groups is decreased, indicating a diminished capacity for endothelial cells to recruit macrophages (Fig. S48). Although these anti-inflammation effects are observed in both Nb₂C-aOPN and Nb₂C-aOPN + NIR group, there is minimal change in the plaque size or the components of the plaques in the Nb₂C-aOPN group. Previous studies have demonstrated that anti-inflammatory strategies, such as tumor necrosis factor- α blockade and statins (known as lipid-lowering medicines), can reduce inflammation and stabilize plaques, yet their impact on plaque regression remains uncertain [61]. It is worth noting that the twelve-week high cholesterol feed used in this study represents a late-stage atherosclerotic plaque, characterized by a plateau in plaque size. This suggests that the induction of plaque regression through anti-inflammatory strategy, referring to Nb₂C-aOPN group in this study, may not be effectively achieved within a limited duration, which is aligned with the previous studies [62,63]. In conjunction with the results observed on *in vitro* experiments, we propose that the decrease in plaque volume is primarily due to photothermal ablation, while the anti-inflammation effect may contribute to prolonged plaque regression.

Atherosclerosis is a systemic disease, characterized by the development of atherosclerotic plaques primarily in the branches and curvatures of the arteries. In this study, we employed a 1 cm diameter laser for a proof-of-concept experiment. The NIR treatment range encompassed the carotid arteries, aortic arches and thoracic aortas, where a reduction in plaque size was observed (Fig. 7b). In contrast, the abdominal aortas show no reduction in plaque size due to the absence of NIR light exposure (Fig. S49). We acknowledge the limited effect on plaque reduction in other arterial regions due to the restricted coverage range of the current light source. To address this issue, we propose the use of a light

source with a larger irradiation range in future studies, such as an 808 nm LED lamp, to expand the irradiation and treatment area. Infrared LED lamps are frequently used in clinical physical therapy and are generally considered safe, but it is crucial to adhere to appropriate usage methods and dosages. Excessive exposure should be avoided to prevent skin burns, and these potential issues must be closely monitored and evaluated in further studies to ensure both the safety and efficacy of the treatment. Despite this limitation, our approach retains significant utility, as different pathological stages of atherosclerosis necessitate distinct therapeutic strategies. Our therapy employed Nb₂C-aOPN to precisely detect vulnerable plaques, enabling targeted interventions at critical locations. This capability is of considerable practical importance, as it facilitates the early identification and focused treatment of high-risk areas within the vascular system. Furthermore, the short-term intervention demonstrated in our study offers several advantages over traditional treatment modalities. It proves to be more efficient and cost-effective compared to prolonged pharmacological treatments and presents a safer alternative to invasive surgical procedures. These attributes make our therapeutic approach a valuable addition to current atherosclerosis management strategies, particularly in preventing acute cardiovascular events by addressing critical lesions proactively.

Moreover, there is no discernible difference in body weight (Fig. S50) and blood lipid levels (Fig. 7j and S51) among the mice in these groups. Moreover, throughout the course of photothermal ablation therapy and in the post-treatment period, no symptoms, such as limb paralysis or motor coordination issues potentially caused by plaque detachment, have been observed. Histological analysis of major organs shows negligible pathological toxicity in the Nb₂C-aOPN + NIR group (Fig. S52).

3. Conclusion

In summary, the development and biomedical application of Nb₂C-aOPN mark a significant advancement in nano-theranostics for targeted atherosclerosis treatment. This study successfully combines the benefits of photothermal therapy and anti-inflammatory strategies, using the Nb₂C-based MXenzyme to provide the direct evidence for promotion of atherosclerotic plaque regression. The strategically engineered Nb₂C-aOPN MXenzyme not only facilitates mild photothermal ablation of foam cells, but also effectively reduces inflammation in the plaque microenvironment. Importantly, Nb₂C-aOPN plays a pivotal role in detecting vulnerable plaques and monitoring atherosclerotic lesions through photoacoustic imaging. This comprehensive approach represents substantial progress in tackling the intricate pathophysiology of atherosclerosis and lays the groundwork for developing multifunctional 2D MXenzyme-based nanomedicine for lipid metabolism disorders, including atherosclerosis, obesity, and non-alcoholic fatty liver disease.

4. Materials and methods

The detailed experimental methods were described in Supporting Information.

Ethics approval and consent to participate

The animal experiments were approved by the Shanghai General Hospital Clinical Center Laboratory Animal Welfare & Ethics Committee (License number: 2023AW017). All animal experiment procedures were performed in accordance with the Animal Management Rules of the Ministry of Health of the P. R. of China and the Guidelines for the Care and Use of Laboratory Animals of China.

CRedit authorship contribution statement

Wenqi Pan: Writing – review & editing, Writing – original draft, Visualization, Validation, Software, Resources, Project administration,

Methodology, Investigation, Formal analysis, Data curation, Conceptualization. **Jingyun Cheng**: Writing – original draft, Visualization, Validation, Resources, Methodology, Investigation, Formal analysis, Data curation. **Xinyue Cao**: Writing – original draft, Visualization, Validation, Software, Methodology, Investigation, Formal analysis, Data curation. **Yi Zheng**: Writing – original draft, Visualization, Validation, Resources, Methodology, Investigation, Formal analysis, Data curation. **Zhenyu Yang**: Writing – original draft, Visualization, Software, Methodology, Investigation, Formal analysis, Data curation. **Wei Feng**: Writing – review & editing, Writing – original draft, Visualization, Validation, Supervision, Software, Resources, Project administration, Methodology, Investigation, Funding acquisition, Formal analysis, Data curation, Conceptualization. **Yu Chen**: Writing – review & editing, Writing – original draft, Visualization, Validation, Supervision, Software, Resources, Project administration, Methodology, Investigation, Funding acquisition, Formal analysis, Data curation, Conceptualization. **Rong Wu**: Writing – review & editing, Writing – original draft, Visualization, Validation, Supervision, Software, Resources, Project administration, Methodology, Investigation, Funding acquisition, Formal analysis, Data curation, Conceptualization.

Declaration of competing interest

The authors declare that they have no known competing financial interests or personal relationships that could have appeared to influence the work reported in this paper.

Acknowledgements

This work was supported by National Natural Science Foundation of China (Grants No. 82071931, 82130057), National Key Research and Development Projects (Grants No. 2022YFC3602400), program from Science and Technology Commission of Shanghai Municipality (Grants No. 20Y11912400), Shanghai Science and Technology Program (Grant No. 21010500100), Basic Research Program of Shanghai Municipal Government (Grant No. 21JC1406002), Shanghai Science and Technology Committee Rising-Star Program (Grant No. 210A1403100), Shanghai Science and Technology Committee Biomedical Program (Grant No. 23S11900900), Wenzhou Basic Scientific Research Project (Grant No. Y20220138), “Shuguang Program” supported by Shanghai Education Development Foundation and Shanghai Municipal Education Commission (Grant No. 21SG39) and Innovative research team of high-level local universities in Shanghai.

Appendix A. Supplementary data

Supplementary data to this article can be found online at <https://doi.org/10.1016/j.bioactmat.2024.07.001>.

References

- [1] W. Herrington, B. Lacey, P. Sherliker, J. Armitage, S. Lewington, Epidemiology of atherosclerosis and the potential to reduce the global burden of atherothrombotic disease, *Circ. Res.* 118 (4) (2016) 535–546.
- [2] E. Falk, Pathogenesis of atherosclerosis, *J. Am. Coll. Cardiol.* 47 (8 Suppl) (2006) C7–C12.
- [3] P. Libby, The changing landscape of atherosclerosis, *Nature* 592 (7855) (2021) 524–533.
- [4] C. Napoli, V. Crudele, A. Soricelli, M. Al-Omran, N. Vitale, T. Infante, F.P. Mancini, Primary prevention of atherosclerosis: a clinical challenge for the reversal of epigenetic mechanisms? *Circulation* 125 (19) (2012) 2363–2373.
- [5] M.B. Mortensen, A. Tybjaerg-Hansen, B.G. Nordestgaard, Statin eligibility for primary prevention of cardiovascular disease according to 2021 European prevention guidelines compared with other international guidelines, *JAMA Cardiol* 7 (8) (2022) 836–843.
- [6] K.I. Paraskevas, P. Glaviczi, P.L. Antignani, A.J. Comerota, A. Dardik, A. H. Davies, H.H. Eckstein, G. Faggioli, E.F.J. Fernandes, G. Fraedrich, G. Geroulakos, J. Gollidge, A. Gupta, V.S. Gurevich, A. Jawien, M.K. Jezovnik, S. K. Kakkos, M. Knoflach, G. Lanza, C.D. Liapis, I.M. Loftus, A. Mansilha, A. N. Nicolaides, R. Pini, P. Poredos, R.M. Proczka, J.B. Ricco, T. Rundek, L. Saba, F. Schlachetzki, M. Silvestrini, F. Spinelli, F. Stilo, J.S. Suri, A.V. Svetlikov, C. J. Zeebregts, S. Chaturvedi, F.J. Veith, D.P. Mikhailidis, Benefits and drawbacks of statins and non-statin lipid lowering agents in carotid artery disease, *Prog. Cardiovasc. Dis.* 73 (2022) 41–47.
- [7] T.G. Brott, R.D. Brown Jr., F.B. Meyer, D.A. Miller, H.J. Cloft, T.M. Sullivan, Carotid revascularization for prevention of stroke: carotid endarterectomy and carotid artery stenting, *Mayo Clin. Proc.* 79 (9) (2004) 1197–1208.
- [8] F. Litvack, W.S. Grundfest, J. Segalowitz, T. Papaioanniu, T. Goldenberg, J. Laudenslager, L. Hestrin, J.S. Forrester, N.A. Eigler, S. Cook, Interventional cardiovascular therapy by laser and thermal angioplasty, *Circulation* 81 (3 Suppl) (1990) Iv109–Iv116.
- [9] Y.-S. Xu, Z.-P. Yao, T.-Q. Zhao, Y.-R. Gu, X. Zhang, P. Song, MXene/dendritic co/polyvinylidene fluoride composite photothermal membrane: preparation and interfacial evaporation properties, *Chin. J. Inorg. Chem.* 38 (12) (2022) 2423–2432.
- [10] J. Chen, T. Chen, Q. Fang, C. Pan, O.U. Akakuru, W. Ren, J. Lin, A. Sheng, X. Ma, A. Wu, Gd(2)O(3)/b-TiO(2) composite nanoprobe with ultra-high photoconversion efficiency for MR image-guided NIR-II photothermal therapy, *Explorations* 2 (6) (2022) 20220014.
- [11] X. Wang, X. Wu, J. Qin, K. Ye, F. Lai, B. Li, G. He, X. Lu, D.J.L. Brett, I.P. Parkin, Differential phagocytosis-based photothermal ablation of inflammatory macrophages in atherosclerotic disease, *ACS Appl. Mater. Interfaces* 11 (44) (2019) 41009–41018.
- [12] X. Li, R. Wu, H. Chen, T. Li, H. Jiang, X. Xu, X. Tang, M. Wan, C. Mao, D. Shi, Near-infrared light-driven multifunctional tubular micromotors for treatment of atherosclerosis, *ACS Appl. Mater. Interfaces* 13 (26) (2021) 30930–30940.
- [13] Z. Cao, G. Yuan, L. Zeng, L. Bai, X. Liu, M. Wu, R. Sun, Z. Chen, Y. Jiang, Q. Gao, Y. Chen, Y. Zhang, Y. Pan, J. Wang, Macrophage-targeted sonodynamic/photothermal synergistic therapy for preventing atherosclerotic plaque progression using CuS/TiO(2) heterostructured nanosheets, *ACS Nano* 16 (7) (2022) 10608–10622.
- [14] T. Dai, W. He, S. Tu, J. Han, B. Yuan, C. Yao, W. Ren, A. Wu, Black TiO(2) nanoprobe-mediated mild phototherapy reduces intracellular lipid levels in atherosclerotic foam cells via cholesterol regulation pathways instead of apoptosis, *Bioact. Mater.* 17 (2022) 18–28.
- [15] H. Liu, H. Wang, Q. Li, Y. Wang, Y. He, X. Li, C. Sun, O. Ergonul, F. Can, Z. Pang, B. Zhang, Y. Hu, LPS adsorption and inflammation alleviation by polymyxin B-modified liposomes for atherosclerosis treatment, *Acta Pharm. Sin. B* 13 (9) (2023) 3817–3833.
- [16] J. Yang, R. Zhang, H. Zhao, H. Qi, J. Li, J.F. Li, X. Zhou, A. Wang, K. Fan, X. Yan, T. Zhang, Bioinspired copper single-atom nanozyme as a superoxide dismutase-like antioxidant for sepsis treatment, *Explorations* 2 (4) (2022) 20210267.
- [17] D. Jiang, D. Ni, Z.T. Rosenkrans, P. Huang, X. Yan, W. Cai, Nanozyme: new horizons for responsive biomedical applications, *Chem. Soc. Rev.* 48 (14) (2019) 3683–3704.
- [18] S. Zhang, Y. Li, S. Sun, L. Liu, X. Mu, S. Liu, M. Jiao, X. Chen, K. Chen, H. Ma, T. Li, X. Liu, H. Wang, J. Zhang, J. Yang, X.D. Zhang, Single-atom nanozymes catalytically surpassing naturally occurring enzymes as sustained stitching for brain trauma, *Nat. Commun.* 13 (1) (2022) 4744.
- [19] B. Yang, H. Yao, J. Yang, C. Chen, J. Shi, Construction of a two-dimensional artificial antioxidant for nanocatalytic rheumatoid arthritis treatment, *Nat. Commun.* 13 (1) (2022) 1988.
- [20] J. Mu, C. Li, Y. Shi, G. Liu, J. Zou, D.Y. Zhang, C. Jiang, X. Wang, L. He, P. Huang, Y. Yin, X. Chen, Protective effect of platinum nano-antioxidant and nitric oxide against hepatic ischemia-reperfusion injury, *Nat. Commun.* 13 (1) (2022) 2513.
- [21] R. Hu, C. Dai, C. Dong, L. Ding, H. Huang, Y. Chen, B. Zhang, Living macrophage-delivered tetrapod PdH nanoenzyme for targeted atherosclerosis management by ROS scavenging, hydrogen anti-inflammation, and autophagy activation, *ACS Nano* 16 (10) (2022) 15959–15976.
- [22] M. Geethika, N. Singh, S. Kumar, S.K.N. Kumar, G. Mugesh, A redox modulatory sod mimetic nanozyme prevents the formation of cytotoxic peroxy nitrite and improves nitric oxide bioavailability in human endothelial cells, *Adv. Healthcare Mater.* (2023) e2300621.
- [23] X. Fu, X. Yu, J. Jiang, J. Yang, L. Chen, Z. Yang, C. Yu, Small molecule-assisted assembly of multifunctional ceria nanozymes for synergistic treatment of atherosclerosis, *Nat. Commun.* 13 (1) (2022) 6528.
- [24] W. Liu, Y. Zhang, G. Wei, M. Zhang, T. Li, Q. Liu, Z. Zhou, Y. Du, H. Wei, Integrated cascade nanozymes with antisense activities for atherosclerosis therapy, *Angew. Chem. Int. Ed.* 62 (33) (2023) e202304465.
- [25] J.W. Song, J.W. Ahn, M.W. Lee, H.J. Kim, D.O. Kang, R.H. Kim, U.G. Kang, Y. H. Kim, J. Han, Y.H. Park, H.S. Nam, H. Yoo, K. Park, J.W. Kim, Targeted theranostic photoactivation on atherosclerosis, *J. Nanobiotechnol.* 19 (1) (2021) 338.
- [26] S. Zhang, Y. Liu, Y. Cao, S. Zhang, J. Sun, Y. Wang, S. Song, H. Zhang, Targeting the microenvironment of vulnerable atherosclerotic plaques: an emerging diagnosis and therapy strategy for atherosclerosis, *Adv. Mater.* 34 (29) (2022) e2110660.
- [27] Q. Li, Z. Huang, Z. Pang, Q. Wang, J. Gao, J. Chen, Z. Wang, H. Tan, S. Li, F. Xu, J. Chen, M. Liu, X. Weng, H. Yang, Y. Song, J. Qian, J. Ge, Targeted delivery of platelet membrane modified extracellular vesicles into atherosclerotic plaque to regress atherosclerosis, *Chin. J. Chem.* 452 (2023).
- [28] Y. Song, N. Zhang, Q. Li, J. Chen, Q. Wang, H. Yang, H. Tan, J. Gao, Z. Dong, Z. Pang, Z. Huang, J. Qian, J. Ge, Biomimetic liposomes hybrid with platelet membranes for targeted therapy of atherosclerosis, *Chin. J. Chem.* 408 (2021).
- [29] K. Shirakawa, M. Sano, Osteopontin in cardiovascular diseases, *Biomolecules* 11 (7) (2021).

- [30] N.P.E. Kadoglou, E. Khattab, N. Velidakis, E. Gkougloudi, The role of osteopontin in atherosclerosis and its clinical manifestations (atherosclerotic cardiovascular diseases)-a narrative review, *Biomedicines* 11 (12) (2023).
- [31] X. Luo, J. Shi, R. Wang, L. Cao, Y. Gao, J. Wang, M. Hong, X. Sun, Y. Zhang, Near-Infrared persistent luminescence nanoprobe for early detection of atherosclerotic plaque, *ACS Nano* 18 (8) (2024) 6500–6512.
- [32] S. Li, T. Gou, Q. Wang, M. Chen, Z. Chen, M. Xu, Y. Wang, D. Han, R. Cao, J. Liu, P. Liang, Z. Dai, F. Cao, Ultrasound/optical dual-modality imaging for evaluation of vulnerable atherosclerotic plaques with osteopontin targeted nanoparticles, *Macromol. Biosci.* 20 (2) (2020) e1900279.
- [33] Q. Fu, R. Zhu, J. Song, H. Yang, X. Chen, Photoacoustic imaging: contrast agents and their biomedical applications, *Adv. Mater.* 31 (6) (2019) e1805875.
- [34] J. Mi, D. Cui, Z. Zhang, G. Mu, Y. Shi, NIR-II femtosecond laser ignites MXene as photoacoustic bomb for continuous high-precision tumor blasting, *Nanoscale* 15 (41) (2023) 16539–16551.
- [35] H. Lin, S. Gao, C. Dai, Y. Chen, J. Shi, A two-dimensional biodegradable niobium carbide (MXene) for photothermal tumor eradication in NIR-I and NIR-II biowindows, *J. Am. Chem. Soc.* 139 (45) (2017) 16235–16247.
- [36] W. Feng, X. Han, H. Hu, M. Chang, L. Ding, H. Xiang, Y. Chen, Y. Li, 2D vanadium carbide MXene to alleviate ROS-mediated inflammatory and neurodegenerative diseases, *Nat. Commun.* 12 (1) (2021) 2203.
- [37] P. Zhang, L. Wang, K. Du, S. Wang, Z. Huang, L. Yuan, Z. Li, H. Wang, L. Zheng, Z. Chai, W. Shi, Effective removal of U(VI) and Eu(III) by carboxyl functionalized MXene nanosheets, *J. Hazard Mater.* 396 (2020) 122731.
- [38] X. Ge, H. Cui, J. Kong, S.Y. Lu, R. Zhan, J. Gao, Y. Xu, S. Lin, K. Meng, L. Zu, S. Guo, L. Zheng, A non-invasive nanoprobe for in vivo photoacoustic imaging of vulnerable atherosclerotic plaque, *Adv. Mater.* 32 (38) (2020) e2000037.
- [39] W. Zhen, Y. Liu, L. Lin, J. Bai, X. Jia, H. Tian, X. Jiang, BSA-IrO₂ : catalase-like nanoparticles with high photothermal conversion efficiency and a high X-ray absorption coefficient for anti-inflammation and Antitumor theranostics, *Angew. Chem. Int. Ed.* 57 (32) (2018) 10309–10313.
- [40] H. Yang, L. Xia, X. Ye, J. Xu, T. Liu, L. Wang, S. Zhang, W. Feng, D. Du, Y. Chen, Ultrathin niobium carbide MXene for remedying hypertension by antioxidative and neuroprotective actions, *Angew. Chem. Int. Ed.* 62 (26) (2023) e202303539.
- [41] C. Du, W. Feng, X. Dai, J. Wang, D. Geng, X. Li, Y. Chen, J. Zhang, Cu(2+) -chelatable and ROS-scavenging MXene as NIR-II-triggered blood-brain barrier-crossing nanocatalyst against alzheimer's disease, *Small* 18 (39) (2022) e2203031.
- [42] J. Liu, W. Lu, X. Lu, L. Zhang, H. Dong, Y. Li, Versatile Ti(3)C₂T_x MXene for free-radical scavenging, *Nano Res.* 15 (3) (2022) 2558–2566.
- [43] X. Ren, M. Huo, M. Wang, H. Lin, X. Zhang, J. Yin, Y. Chen, H. Chen, Highly catalytic niobium carbide (MXene) promotes hematopoietic recovery after radiation by free radical scavenging, *ACS Nano* 13 (6) (2019) 6438–6454.
- [44] M. Certo, C.H. Tsai, V. Pucino, P.C. Ho, C. Mauro, Lactate modulation of immune responses in inflammatory versus tumour microenvironments, *Nat. Rev. Immunol.* 21 (3) (2021) 151–161.
- [45] M. Naghavi, R. John, S. Naguib, M.S. Siadaty, R. Grasu, K.C. Kurian, W.B. van Winkle, B. Soller, S. Litovsky, M. Madjid, J.T. Willerson, W. Casscells, pH Heterogeneity of human and rabbit atherosclerotic plaques; a new insight into detection of vulnerable plaque, *Atherosclerosis* 164 (1) (2002) 27–35.
- [46] A.R. Tall, L. Yvan-Charvet, Cholesterol, inflammation and innate immunity, *Nat. Rev. Immunol.* 15 (2) (2015) 104–116.
- [47] Y. Li, D. Wang, X. Ping, Y. Zhang, T. Zhang, L. Wang, L. Jin, W. Zhao, M. Guo, F. Shen, M. Meng, X. Chen, Y. Zheng, J. Wang, D. Li, Q. Zhang, C. Hu, L. Xu, X. Ma, Local hyperthermia therapy induces browning of white fat and treats obesity, *Cell* 185 (6) (2022) 949–966.e19.
- [48] R. Rosenzweig, N.B. Nillegoda, M.P. Mayer, B. Bukau, The Hsp70 chaperone network, *Nat. Rev. Mol. Cell Biol.* 20 (11) (2019) 665–680.
- [49] B. Gungor, L. Vanharanta, M. Hölltä-Vuori, J. Pirhonen, N.H.T. Petersen, S. Gramolelli, P.M. Ojala, T. Kirkegaard, E. Ikonen, HSP70 induces liver X receptor pathway activation and cholesterol reduction in vitro and in vivo, *Mol. Metabol.* 28 (2019) 135–143.
- [50] M.A. Kennedy, G.C. Barrera, K. Nakamura, A. Baldán, P. Tarr, M.C. Fishbein, J. Frank, O.L. Francone, P.A. Edwards, ABCG1 has a critical role in mediating cholesterol efflux to HDL and preventing cellular lipid accumulation, *Cell Metabol.* 1 (2) (2005) 121–131.
- [51] N.R. Madamanchi, M.S. Runge, Mitochondrial dysfunction in atherosclerosis, *Circ. Res.* 100 (4) (2007) 460–473.
- [52] R. Kityk, J. Kopp, M.P. Mayer, Molecular mechanism of J-domain-triggered ATP hydrolysis by Hsp70 chaperones, *Mol. Cell* 69 (2) (2018) 227–237.e4.
- [53] X. Xin, T. Gong, Y. Hong, Hydrogen peroxide initiates oxidative stress and proteomic alterations in meningotheial cells, *Sci. Rep.* 12 (1) (2022) 14519.
- [54] A. Płóciennikowska, A. Hromada-Judycka, K. Borzęcka, K. Kwiatkowska, Co-operation of TLR4 and raft proteins in LPS-induced pro-inflammatory signaling, *Cell. Mol. Life Sci.* 72 (3) (2015) 557–581.
- [55] I.S. Afonina, Z. Zhong, M. Karin, R. Beyaert, Limiting inflammation-the negative regulation of NF- κ B and the NLRP3 inflammasome, *Nat. Immunol.* 18 (8) (2017) 861–869.
- [56] R. Pai, H. Ha, M.A. Kirschenbaum, V.S. Kamanna, Role of tumor necrosis factor-alpha on mesangial cell MCP-1 expression and monocyte migration: mechanisms mediated by signal transduction, *J. Am. Soc. Nephrol.* 7 (6) (1996) 914–923.
- [57] P. Miossec, J.K. Kolls, Targeting IL-17 and TH17 cells in chronic inflammation, *Nat. Rev. Drug Discov.* 11 (10) (2012) 763–776.
- [58] P. Gaba, B.J. Gersh, J. Muller, J. Narula, G.W. Stone, Evolving concepts of the vulnerable atherosclerotic plaque and the vulnerable patient: implications for patient care and future research, *Nat. Rev. Cardiol.* 20 (3) (2023) 181–196.
- [59] R. Lassila, Inflammation in atheroma: implications for plaque rupture and platelet-collagen interaction, *Eur. Heart J.* 14 (Suppl K) (1993) 94–97.
- [60] S. Stein, J. Weber, S. Nasser-Stein, J. Pahl, H.E. Zhang, S.A. Mohammed, S. Oppi, D.S. Gaul, F. Paneni, A. Tailleux, B. Staels, F. von Meyenn, F. Ruschitzka, M. D. Gorrell, T.F. Lüscher, C.M. Matter, Deletion of fibroblast activation protein provides atheroprotection, *Cardiovasc. Res.* 117 (4) (2021) 1060–1069.
- [61] R. Klingenberg, G.K. Hansson, Treating inflammation in atherosclerotic cardiovascular disease: emerging therapies, *Eur. Heart J.* 30 (23) (2009) 2838–2844.
- [62] P.M. Ridker, B.M. Everett, A. Pradhan, J.G. MacFadyen, D.H. Solomon, E. Zaharris, V. Mam, A. Hasan, Y. Rosenberg, E. Iturriaga, M. Gupta, M. Tsigoulis, S. Verma, M. Clearfield, P. Libby, S.Z. Goldhaber, R. Seagle, C. Ofori, M. Saklayen, S. Butman, N. Singh, M. Le May, O. Bertrand, J. Johnston, N.P. Paynter, R.J. Glynn, Low-dose methotrexate for the prevention of atherosclerotic events, *N. Engl. J. Med.* 380 (8) (2019) 752–762.
- [63] M.L. O'Donoghue, R. Glaser, M.A. Cavender, P.E. Aylward, M.P. Bonaca, A. Budaj, R.Y. Davies, M. Dellborg, K.A. Fox, J.A. Gutierrez, C. Hamm, R.G. Kiss, F. Kovar, J. F. Kuder, K.A. Im, J.J. Lepore, J.L. Lopez-Sendon, T.O. Ophuis, A. Parkhomenko, J. B. Shannon, J. Spinar, J.F. Tanguay, M. Ruda, P.G. Steg, P. Theroux, S.D. Wiviott, I. Laws, M.S. Sabatine, D.A. Morrow, Effect of losmapimod on cardiovascular outcomes in patients hospitalized with acute myocardial infarction: a randomized clinical trial, *JAMA, J. Am. Med. Assoc.* 315 (15) (2016) 1591–1599.